Lateral Resolution of Electrostatic Force Microscopy

for Mapping of Dielectric Interfaces in Ambient Conditions

M. Labardi [(1,*)] , A. Bertolla[(2)], C. Sollogoub[(3)], R. Casalini[(4)], S. Capaccioli [(1,2,5)]

[1] *CNR-IPCF, Sede Secondaria di Pisa, Largo Pontecorvo 3,56127 Pisa, Italy*

[2] *Dipartimento di Fisica "E. Fermi", Università di Pisa, Largo Pontecorvo 3,56127 Pisa, Italy*

[3] *PIMM, Arts et Metiers Institute of Technology, CNRS, Cnam, HESAM University, 151 Bd. de l'Hopital, 75013 Paris, France*

[4]*Chemistry Division, Naval Research Laboratory, Washington, DC 20375-5320, USA*

[5]*CISUP, Centro per l'Integrazione della Strumentazione dell'Università di Pisa, Lungarno Pacinotti 43, 56126 Pisa, Italy*

[*] *Corresponding author: email* labardi@df.unipi.it

Abstract –The attainable lateral resolution of electrostatic force microscopy (EFM) in ambient air environment on dielectric materials was characterized on a reference sample comprised of two distinct, immiscible glassy polymers cut in the cross-section by ultramicrotomy. Such sample can be modeled as two semi-infinite dielectrics with a sharp interface, presenting a quasi-ideal, sharp dielectric contrast. Electric polarizability line profiles across the interface were obtained, in both lift-mode and feedback-regulated dynamic mode EFM, as a function of probe/surface separation, for different cases of oscillation amplitudes. We find that the results do not match predictions for dielectric samples, but comply well or are even better than predicted for conductive interfaces. A resolution down to 3 nm can be obtained by operating in feedback-regulated EFM realized by adopting constant-excitation frequency-modulation mode. This suggests resolution to be ruled by

the closest approach distance rather than by average separation, even with probe oscillation amplitudes as high as 10 nm. For better comparison with theoretical predictions, effective probe radii and cone aperture angles were derived from approach curves, by also taking into account the finite oscillation amplitude of the probe, by exploiting a data reduction procedure previously devised for the derivation of interatomic potentials.

Introduction. Electrostatic Force Microscopy (EFM) is a generic term for scanning probe methods based on Atomic Force Microscopy (AFM) where the conductive sharp probe is electrically biased, and the effect of electrostatic forces between tip and sample is detected. EFM can be exploited to obtain information on various electrical properties of a surface, like e.g. dielectric polarizability, surface bound charge, and contact potential, on a local scale. Some relevant applications concern the mapping of nanoinclusions in dielectric matrices of nanocomposites [1, 2], detection of injected charges on conductive nanolayers [3], and characterization of semiconductor devices and junctions [4]. Of particular interest, the EFM application to realize local dielectric spectroscopy (LDS) [5], realized with different variants [6, 7, 8], could potentially allow to discriminate dielectric relaxation phenomena on the characteristic length scale of dynamical heterogeneity [9], that in glass-forming materials like polymers amounts to a few nm [10, 11].

The long-range nature of Coulombic forces limits the attainable spatial resolution to several nanometers, opposed to the much higher resolution allowed by short-range forces in AFM, due to chemical interactions and atomic mutual repulsion, which pushes such limit down to a sub-atomic scale [12]. Reports of EFM resolution down to the atomic scale are available, in ultra-high vacuum experiments and concerning surface atomic dipole interactions [13]. Resolution on step-like boundaries between insulating salt layers and the metal substrate beneath was assessed by also comparing EFM detection modes based on force and force gradient [14]. Such refined performance is more difficult to achieve in ambient environment, where surfaces are typically contaminated by adsorbed moisture layers. Nevertheless, physical quantities like e.g. dielectric constant, contact potential difference, and surface charge density, can be relevant to characterize the surface on a nanometer length scale, where a description in terms of band theory and thermodynamics can still result as appropriate. The strive to improve the resolution of local electrical probe techniques, in these systems, is due to the necessity to characterize functional properties of increasingly small electronic devices and junctions, as well as to inspect diffuse interfaces in nanocomposite materials, for energy or sensing applications.

EFM spatial resolution δ can be described, according to well-accepted models with a probe with cylindrical symmetry and a parabolic profile [15], in terms of an apex probe radius R and tip/surface distance d, as for instance:

$$\delta = \frac{8}{3}\sqrt{2Rd}$$ (1)

that is valid in the case of small distance, $d \ll R$, and by assuming, as a resolution criterion, that δ is the lateral displacement necessary to obtain a change of the signal of interest from 10% to 90% of the total change across a discontinuity.

The spatial resolution is typically determined by calculating the electrostatic force between a conductive probe with cylindrical symmetry and a heterogeneous flat sample, divided in two parts, having distinct electric properties, by an ideally sharp interface, as sketched in Fig. 1(a). The calculation is usually simplified by resorting to the Derjaguin approximation [16], that is, assuming all electric field lines parallel to the direction of symmetry. By calculating the electrostatic force as a function of the lateral position of the probe with respect to the location of the interface, a force profile is obtained, whose width provides the resolution δ, as a function of distance d and probe radius R. On condition that $d \ll R$, the Derjaguin approximation provides a good description of the problem [15].

Another common definition for the EFM resolution can be given in terms of the capability to resolve two point-like objects on the surface [17, 18, 19], or in other words, in terms of the width of a point spread function. However, we prefer to adhere to the former one, for the unidimensional case, that allows comparisons with previous results, e.g. the ones reported in Refs. [14, 15].

Contrary to what is obtained for metals, with dielectric materials the electric field penetrates below the surface, and polarization can be induced at buried interfaces, like the ones that can be present in composite materials [20]. Therefore, the bulk structure of the sample can also contribute

to influence imaging resolution, unlike in the case of conducting interfaces. This feature is commonly exploited, for instance, for imaging of sub-surface nanoinclusions in polymeric nanocomposites [1, 2]. Furthermore, the thickness of the dielectric layer h may be large compared to d, as sketched in Fig. 1(b), therefore the Derjaguin approximation becomes insufficient for a correct theoretical description. Indeed, estimations in this case are usually carried out by numerical simulation.

With regard to lateral resolution, as defined as the passage through the step boundary in a dielectric sample structure with translational symmetry along the z axis, like the one in Fig. 1(b), numerical simulations could be, in principle, performed. However, in the case of more realistic samples, the three-dimensional geometry of the interface could be a different one, like e.g. depicted in Fig. 1(c), where phase separation occurs with an unknown geometry, buried below the surface. Imaging of this situation by EFM may lead to deterioration of resolution, due to the thickness change of the component materials within the probed volume. For a reliable assessment of the limit imaging resolution, the latter effect should be avoided, therefore a sample with the structure of Fig. 1(b) should be used, for the most appropriate comparison with estimations.

Another critical point to be considered for the most correct estimation of EFM resolution is related to the probe shape. It is well known that in EFM, interaction of the farther probe parts (like the probe shaft and the AFM cantilever) leads to resolution loss [21]. A force gradient detection method is usually adopted to contrast such degradation, yielding to remarkable rejection of stray contributions, while on the other hand, the bare force detection is strongly affected by the influence of the farther parts of the probe, like the tip shaft and the cantilever [21, 22].

The standard scanning probe operation mode for the detection of force gradients is the frequency-modulated (FM)-AFM [23], where the shift Δf of the resonant frequency of the cantilever oscillation provides information on the force gradient magnitude. Yet, some contributions from the closest part of the probe shaft persist also by using such mode. For this reason, in order to obtain the

most reliable information on the sample from EFM measurements, the probe geometry should be known to the highest detail.
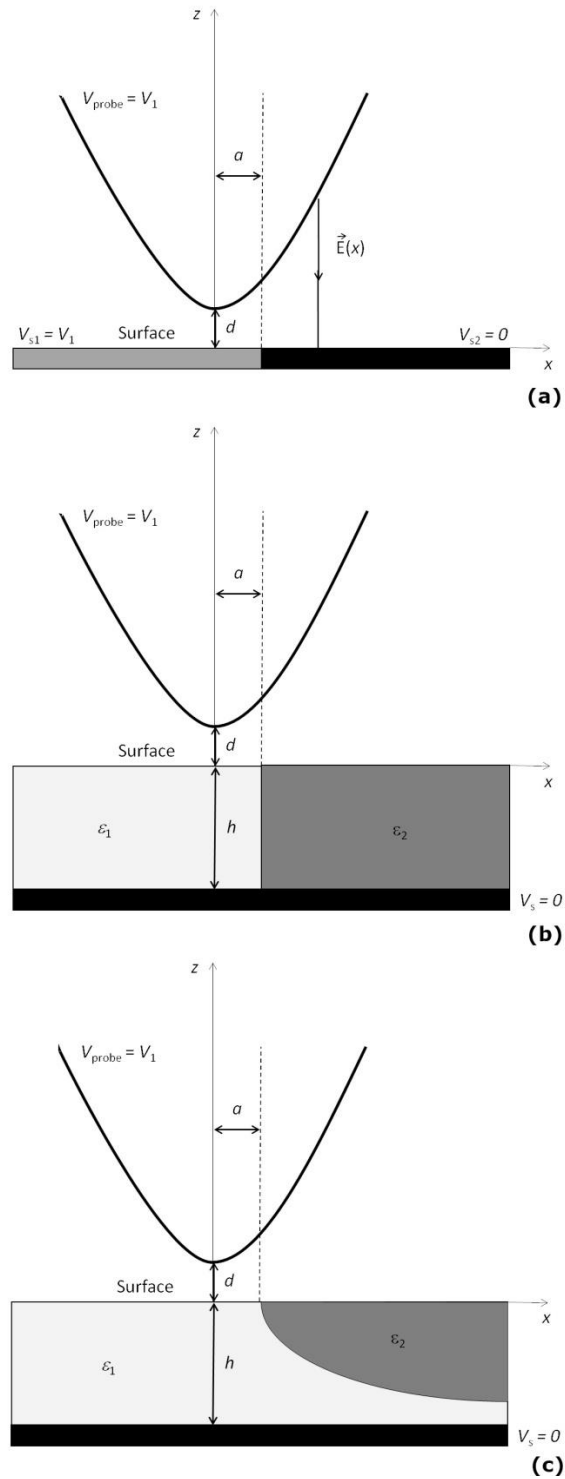
Figure 1: (a) Sketch of probe/surface geometry for calculation of resolution (as from Ref. [15]). (b) Case of two dielectric materials with ideal geometry (symmetry along z), of dielectric constants ε_1 and ε_2, and thickness h. (c) Case of two dielectric materials with unknown buried geometry.

The usual method to characterize the shape of conductive probes is their imaging by scanning electron microscopy (SEM). Inspection of common EFM probes reveals that their geometry is not perfectly reproducible from probe to probe; in particular, the curvature of the shaft close to the apex, as well as the symmetry at the probe edge, are usually not uniform (as visible for instance from the SEM pictures shown in Figure 3 ahead). Although SEM characterization is an important one, especially for checking the probe integrity, or the presence of debris after operation, calibration procedures of the probe performance, concerning specifically electric force detection, are usually carried out by means of the EFM itself. They consist in recording approach curves, where the frequency shift is measured as a function of probe/surface separation L, by using a flat metallic sample [24], and then by best fitting to functions obtained by analytical or numerical calculations, assuming a given probe shape parametrization. This procedure provides *effective* shape parameters for the probe, and releases the necessity of imaging the AFM tips *ex-situ*.

Probe shape can be described in different ways, the most common ones being either a paraboloid shape with apex radius R [15, 21], or a spherical cap with apex radius R and a truncated cone with shaft angle θ_0 [6, 25, 26]. In this work, the last probe shape will be assumed, being more commonly used.

Materials and methods. In order to investigate the inherent limit resolution of EFM on dielectric materials in ambient conditions, we have devised a quasi-ideal dielectric step-contrast surface, where the interface extends in the normal direction through the whole sample thickness. To realize it, we have used a polymer multi-layered film of polystyrene (PS) and poly(lactic acid) (PLA) [27], two immiscible polymers in the glassy state at room temperature, but with different polar character. The multilayer period was chosen as rather large (around 25 μm), in order to obtain well separated interfaces. The multilayer was cross-sectioned by ultramicrotomy, after embedding in microtome resin, by choosing the cutting direction at 45° with respect to the interface direction, for easier

discrimination of those topographic contributions due to the cut from the ones due to the interface itself. The obtained section was applied on a metal sample holder, resulting about 1-2 mm thick.

For both force/distance curves and interface profiling, a Veeco Instruments NanoScope IIIa AFM with MultiMode head was used. EFM was performed by adopting an external AFM controller for frequency modulation (PLLProII, RHK Technology, Troy, USA), based on a phase-locked loop (PLL) detector, optimized to improve EFM performance for local dielectric spectroscopy applications [7, 8]. A voltage $V(t) = V_{ac} \cos(\Omega t)$ was applied to the conductive probes, at a frequency Ω (∼ 80 Hz), and $V_{ac} = 15V_{RMS}$. This rather high value of V_{ac} is necessary for operation on thick dielectric samples compared to thin films, in order to obtain high enough response of the material. Nonetheless, the resulting electric field remains low enough to avoid the onset of nonlinear effects in dielectrics. The value of Ω is chosen as a compromise between scanning speed and S/N ratio, as in previous literature [2, 7, 28].

The frequency shift output $\Delta f(t)$ of the PLL controller was demodulated, at frequency 2Ω, by a dual lock-in amplifier (SRS830DSP, Stanford Research Systems, USA). The amplitude $\Delta f_{2\Omega}$ of such frequency shift modulation depends only on probe/sample capacitance at the current probe position, with no influence from both static charges and contact potential difference [7], allowing more accurate estimations of the dielectric permittivity. All measurements were performed at room temperature and in dry nitrogen gas atmosphere conditions.

Two different scanning modes were used, namely, the lift-mode, customarily used in EFM spectroscopic applications [6] and the FM-AFM at constant excitation (CE) [29], using oscillation amplitude as the signal for distance regulation feedback [30], by means of the same PLL controller. We choose to adopt the latter scheme with the aim to improve lateral resolution of EFM measurements in ambient conditions. Indeed, the use of frequency shift feedback regulation, employed in alternative schemes [31], is usually more critical to be operated in such conditions.

In both AFM operation modes, electric force is detected by recording the frequency shift of the cantilever oscillation caused by the electrostatic force field. In the feedback-regulated mode, an oscillation amplitude A_1 is held constant by the distance feedback regulation (see sketch in Fig. 2), while the tip is concerned also by atomic forces at its oscillation edge, the main ones being due in ambient conditions to capillarity of adsorbed layers, and to atomic repulsion. Such interaction will lead to a shift Δf_{at} due to atomic interactions, that is also measured by the PLL controller. If an electric potential is applied, an additional frequency shift Δf_{el} will occur according to the applied bias. In the lift mode, a topographic profile is recorded during a first (main) pass, by the same way, while applying no bias; during the second (lift) pass, the same profiling is then reproduced at a lifted height, with no need of feedback control. Therefore, during the second pass, the tip is not subjected to the atomic forces anymore, but only to the electric field produced by probe biasing. The tip oscillation A_2 during lift can be changed arbitrarily, from very small to as wide as the tip/sample separation $L = A_1 + h_{lift}$ (Fig. 2); if this condition is exceeded, the tip could impact the surface in an uncontrolled way, so usually this is not done. The closest approach distance z_c is nearly zero under distance feedback-regulation, while it amounts to $A_1 - A_2 + h_{lift}$ during the lift mode second pass (Fig. 2).
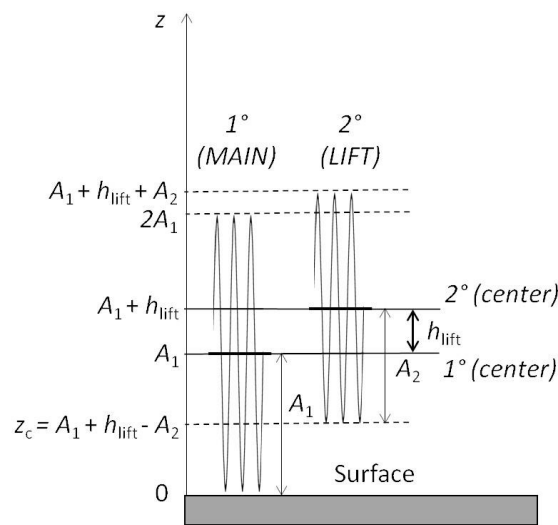
Figure 2. Sketch of the probe oscillation amplitude during feedback-regulated operation (main, amplitude A_1) and lift mode (lift height h_{lift}, amplitude A_2).

Results and discussion.

Probe calibration. We have compared results from three widespread models of AFM tips with a pyramidal shaft, listed in Table I. SEM pictures of such probes are shown in Fig. 3. Approach curves to a flat gold surface, deposited on glass, were recorded for each of these probes, in order to determine their effective probe radius and shaft angle. An example of such approach curve for probe type "χ" is shown in Fig. 4.

Best fitting by one of the models described in Ref. [26], the so-called "straight" model, that showed up here as better modeling our data, was used:

$$F_S^a = -\pi\varepsilon_0 R V^2 \left[\frac{1}{z} - \frac{1}{z + R(1-\sin\theta_0)} - \frac{1}{R}\ln\left(\frac{z + R(1-\sin\theta_0)}{z} \right) \right]$$

$$F_S^c = -\pi\varepsilon_0 V^2 \tan^2\theta_0 \left[\ln\left(\frac{H}{z + R(1-\sin\theta_0)} \right) - 1 + \frac{R\cos^2\theta_0 / \sin\theta_0}{z + R(1-\sin\theta_0)} \right] \tag{2}$$

where the first expression represents the apex term, and the second one the shaft term, with H being the shaft height. The z-derivative of such expressions is used to fit force gradient data therefore the dependence on H is eliminated.

The obtained best-fitting parameters are reported in Table II. It is apparent how probe radii result sometimes different from the values visible in SEM pictures, and especially the shaft angles seem overestimated by this fitting. This is a demonstration of how the electrostatic measurement could give quite different results from what expected from the geometry derived by SEM imaging [26]. However, unrealistic values of angles suggest that there could be a systematic reason why the usual fitting could appear as not accurate enough. We have concentrated on the fact that there might be a dependence on the finite oscillation amplitude A_0 used. Such amplitude cannot be chosen too small during approach curve recording, in order to prevent damage of probes in the event that separation

10

were to decrease too much, due for instance to unwanted thermal drifts. For our measurements, the used amplitudes were $A_0 = 16.5$ nm for the probes "χ" and "η", and 4 nm for the probe "ξ".
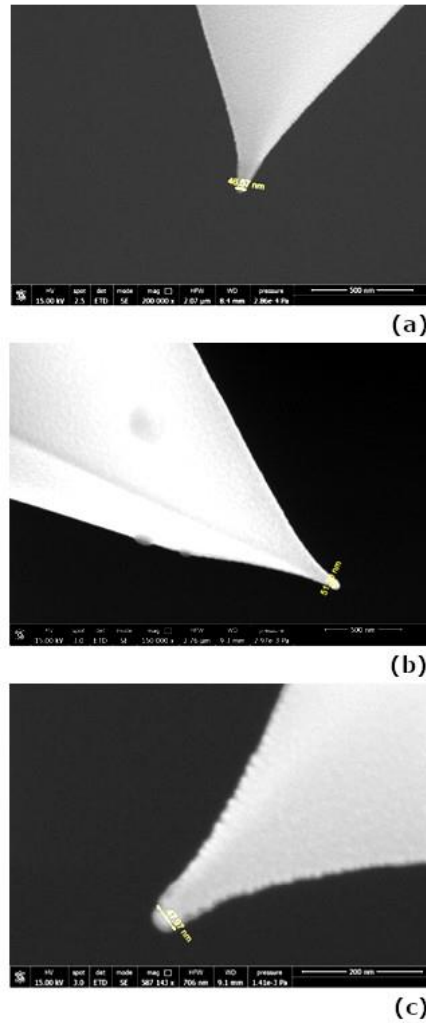
Figure 3: SEM micrographs of the three probes used: (a) Probe "χ", (b) Probe "η", (c) Probe "ξ" (the dimension determined by the SEM micrographs are reported in Table II). Images were taken *after* use.

To take into account the effect of large amplitudes, we have exploited an inversion formula after Sader and Jarvis [32], usually employed to carry out the force/distance dependence from AFM frequency shift data with an excellent precision, by taking into account the finite value of oscillation amplitude. The correction provided by this formula is necessary when the oscillation amplitude spans a substantial part of the interaction potential, since in that case, the applied force changes

11

considerably within the oscillation cycle. Here we apply such method, for the first time to our knowledge, to electrostatic force gradient data. Such inversion formula is expressed as:

$$F(z) = \frac{2k}{\omega_0} \int_z^\infty \left[\left(1 + \frac{A^{1/2}}{8\sqrt{\pi(\zeta - z)}} \right) \Delta\omega(\zeta) - \frac{A^{3/2}}{\sqrt{2(\zeta - z)}} \frac{d\Delta\omega(\zeta)}{d\zeta} \right] d\zeta \tag{3}$$

where $\omega = 2\pi f$. This integration was performed numerically on our approach curve data $\Delta f(L)$.

Label	Brand	Model	Material	k [N/m]	f_0[kHz]
"χ"	NanoSensors	PPP-NCLPt	PtIr5	47	158.03
"η"	MikroMasch	HQ:NSC16/ Cr-Au	Au	45	139.24
"ξ"	MikroMasch	HQ:DPER-XSC11	Pt	42	355.32

Table I. Nominal specifications of the probes used. k is the nominal cantilever spring constant, f_0 the measured free resonant frequency.

Since approach curves were acquired in a distance range of about 500 nm, in order to perform the integration of Eq. (3) including the farther data points we have extrapolated the frequency shift data at large distance by an inverse power term of the form:

$$\Delta\omega_\infty(z) = \frac{\alpha}{z + R(1 - \sin\theta_0)} \tag{4}$$

with the coefficient α adapted in order to join with the acquired data at $z = 500$ nm. This extrapolated function is also shown, as an illustration, for the case of the approach curve of Fig. 4.

The force curve obtained after application of Eq. (3) is then best fitted by the "straight" model for the force (Eq. (2)) [26]. Table II shows also the fitting results with the latter method, while Fig. 5

shows an example of inverted data, with the related best fit curve. It is apparent how fitting quality looks improved with respect to the case of force gradient, and also how the values of shaft angles look now more realistic, while the values of the radii remain sufficiently close to the ones obtained by the previous method. We remark that application of Eq. (3) provides a noticeable effect in such cases when oscillation amplitude is comparable to the interaction range of electrostatic forces, that is, in our case, the tip radius R. Therefore, Eq. (3) is more necessary for tips "χ" and "η", where amplitude $A_0 = 16.5$ nm $\sim R$, while its effect is small for tip "ξ", where $A_0 = 4$nm $<< R$.
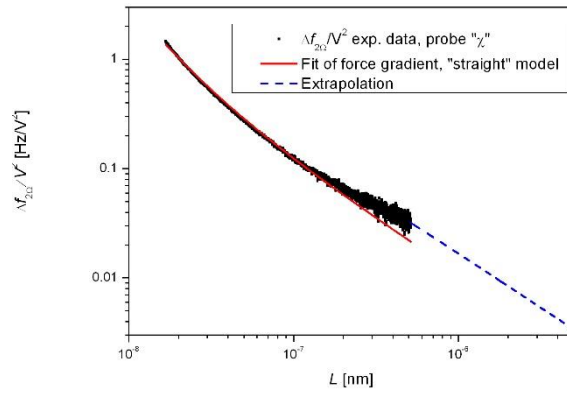
Figure 4: Approach curve for probe "χ", with best fit (red solid line) by the "straight" model (Eq. (2)) for the force gradient [26]. The extrapolated function to allow data integration according to Eq. (3) is also shown (blue dashed line).
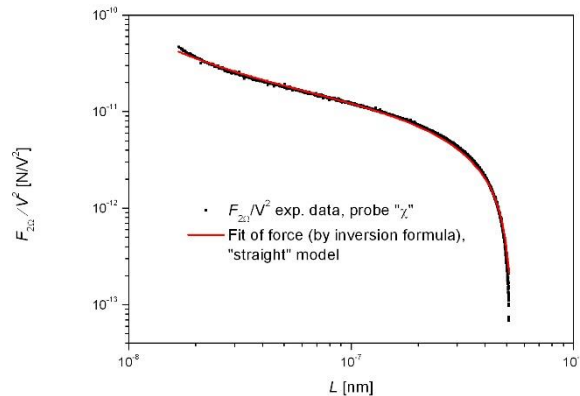
Figure 5: Approach curve for probe "χ", with best fit (red solid line) by the "straight" model (Eq. (2)) for the force. Experimental data were converted from force gradient to force by resorting to the inversion formula of Ref. [32].

Lateral resolution assessment. An example of EFM image of our polymer multilayer sample is shown in Fig. 6. The quality of the obtained cross-section is shown in the AFM topography map of Fig. 6(a), where the almost vertical line visible in the center is located in the proximity of the interface. The inclined lines are instead the scratches from the microtome knife. The corresponding electric contrast image is shown in Fig. 6(b), where the higher dielectric constant of PLA (2.3 at 80 Hz frequency and room temperature) compared to that of PS (2.0) translates into a higher electric signal (brighter region). Dielectric constants differ by 15%, while a contrast of 18% (lift mode) to 19.5% (CE-FM mode) was obtained in electric images. This difference is expected in EFM, since the capacitance depends on the dielectric constant in a non-linear way [26, 33].

| Label	R_{SEM} [nm]	$\theta_{0,SEM}$ [rad] (approx.)	R_{FIT} [nm] (gradient)	$\theta_{0,FIT}$ [rad] (gradient)	R_{FIT} [nm] (force)	$\theta_{0,FIT}$ [rad] (force)
"χ"	23.3	0.3-0.45	23.2	0.97	33.4	0.48
"η"	25.8	0.35	57.8	1 (limit)	42.9	0.57
"ξ"	23.9	0.35-0.45	20.3	1 (limit)	22.8	0.49

Table II. Results of the best fit with the "straight" model for the three probes, in the cases of gradient model (Ref. [26]) and force model by inversion (here introduced). Values of shaft angle turn out as more consistent with the geometry resulting from SEM imaging for the latter model. Note that θ_0 had an upper constraint of 1 rad in these fittings, that however was reached only in the case of the gradient model.

An example of high resolution profile scanning across the interface is shown in Fig. 7(a) (topography) and Fig. 7(b) (electric). The total scan width was 1 μm here, with 512 sampling points, for a limit point-to-point resolution of about 2 nm. An example of electric signal profile is also shown, along with the corresponding topographic trace (Fig. 7(c)), showing a roughness of about 2 nm$_{RMS}$. Sample flatness is important in order to reduce the effect of topography crosstalk on EFM images [34].

Electric traces were fitted by a sigmoidal function:

$$S(x) = a_1 + \frac{a_2 - a_1}{1 + e^{-x/\delta_s}}$$ (5)

with the two asymptotic values a_1 and a_2 as well as the resolution δ_s left as free fitting parameters (it can be shown that the 10%-90% resolution δ amounts in this case to $4.4\delta_s$). The fitting function plot is also reported in Fig. 7(c). The correspondence with the electric image is evident, while no relation with the topographic profile can be noticed.
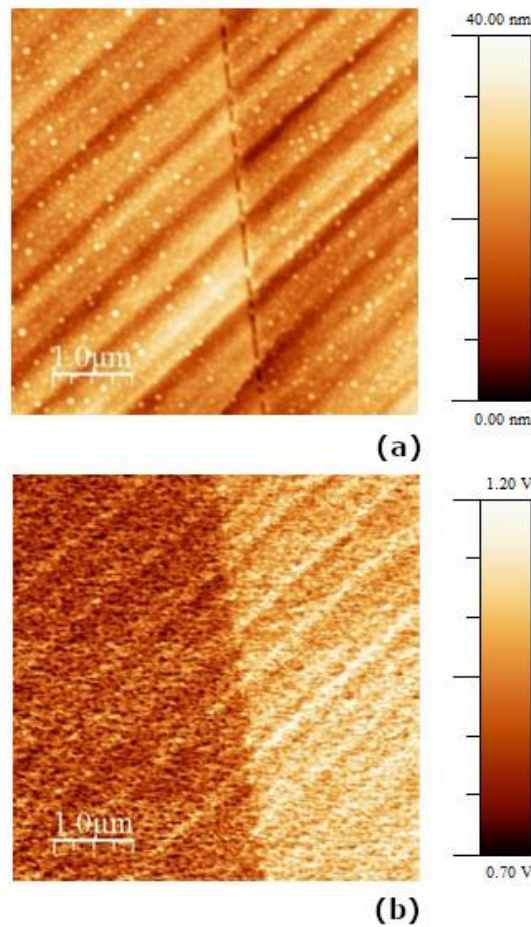
Figure 6: (a) Topography of the multilayered polymer sample. (b) Electric amplitude image (in arbitrary units). PLA (right side) exhibits higher polarizability than PS (left side). The diagonal lines indicate the scratches due to the microtome. The vertical line is located near the demarcation between the two polymers (PS and PLA). The scanning time for this image, acquired with an oscillation amplitude $A_2 = 4$nm in lift mode, was 4800s.

Results of profile fittings are shown in Fig. 8, for various distances, for the three tip models used. Resolution obtained in lift mode is found generally to be consistent, or even better, than theoretical expectations of Eq. (1). The dashed lines in Fig. 8 report the prediction of Eq. (1), as calculated for the probe radius derived from SEM images, while the dotted lines refer to the tip radii derived from our probe calibration procedures. For the first probe model ("χ"), oscillated with an amplitude $A_2 =$ 4 nm in lift mode, experimental resolution (open symbols) is systematically better than predictions.
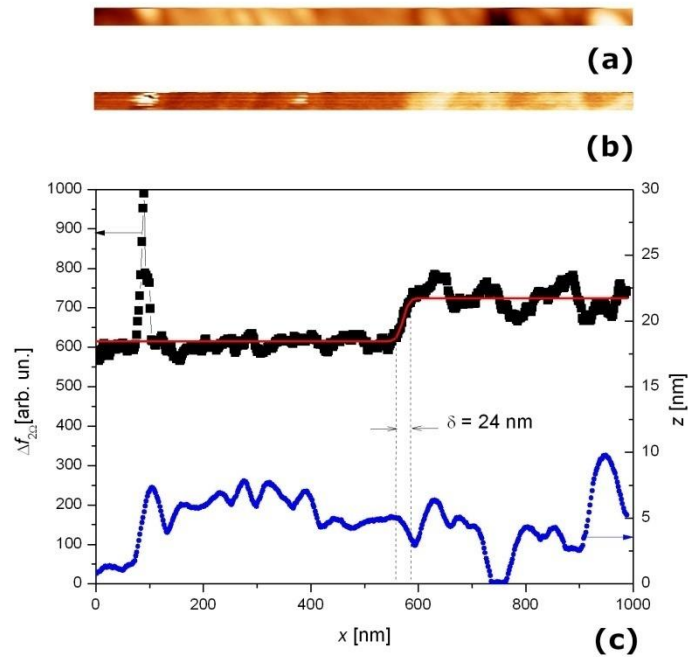
Figure 7: (a) Topography and (b) corresponding electric permittivity image of the test sample, obtained in lift mode by probe "χ", showing the sharp transition between the two polymers (images are shown just for illustration purpose. Image width is 1000 nm, the scale bars are the same than in Fig. 6). The scanning time for these images, acquired with an oscillation amplitude $A_2 =$ 4nm in lift mode, was 600s. (c) (top) Line profile taken from image (b), along with its fitting curve by the sigmoidal function of Eq. (5), showing dielectric contrast of 18% and lateral resolution of 24 nm. (bottom) Line profile of topography, taken from image (a), showing poor correlation with the electric permittivity profile.
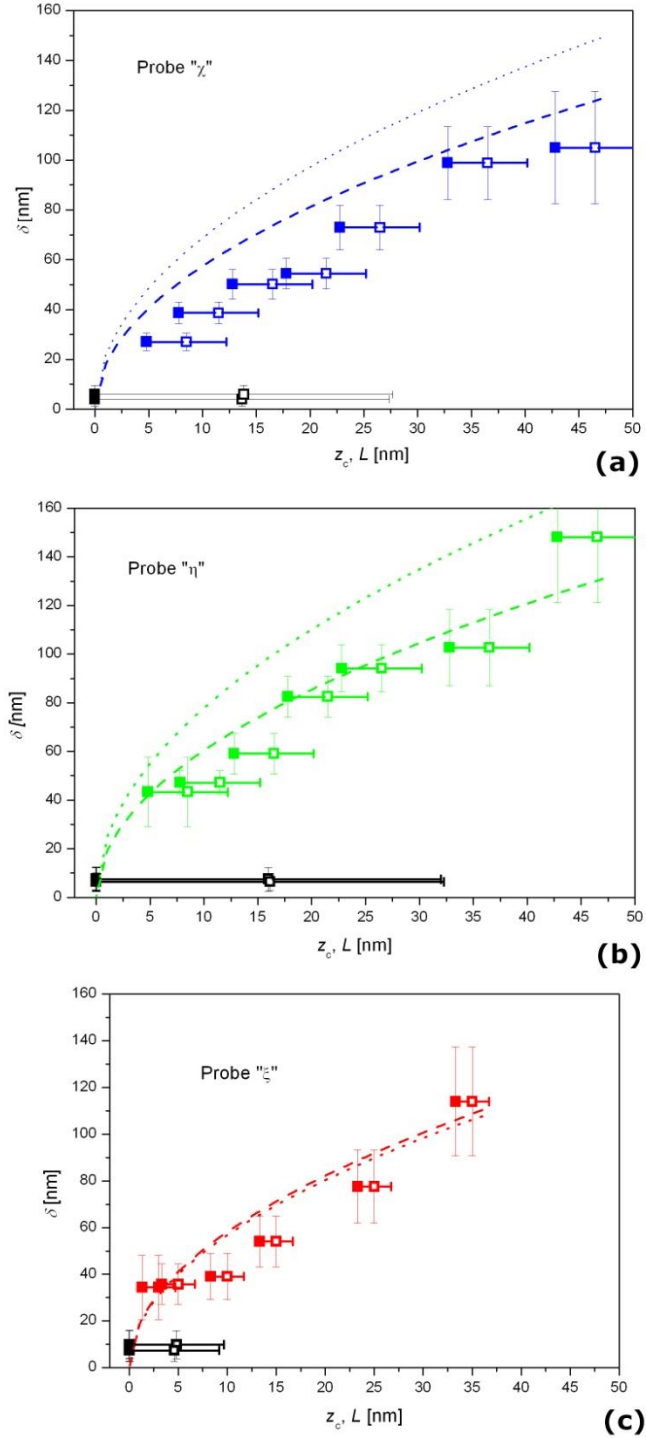
Figure 8. Resolution obtained in lift mode (colored hollow squares) and feedback-regulated mode (black hollow squares) as a function of separation L, for the three different probe types (see Table I): (a) probe "χ", (b) probe "η", (c) probe "ξ". The lines represent the 10%-90% resolution expected according to Eq. (1) and the tip radii derived from both SEM pictures (dashed line) and "straight" force model (dotted line). Full symbols correspond to the same data plotted as a function of closest approach distance z_c. Horizontal bars indicate the span of the used oscillation amplitude. Vertical bars indicate statistical errors on the fitting results, derived from averaging over 5 line profiles for each case.

For the second probe model ("η"), with $A_2 = 4$ nm, the agreement with estimations is better. The third probe ("ξ") was oscillated with a smaller amplitude ($A_2 = 2$ nm), and also provides good agreement. From these results, it could be concluded that theoretical estimations for constant-potential surfaces also describe with good accuracy the case of dielectric surfaces.

Numerical simulations of EFM resolution on thick dielectric samples (Ref. [17]) predict a linear trend with probe/sample distance, instead of a square root dependence like Eq. (1). In particular, a finite value of resolution is predicted, by such calculations, even at zero distance. By only considering the points obtained in lift mode, our results could also be consistent with such a trend, since they could be fitted by a linear function as well. However, a further observation, that turned out to be the most important one in our investigation, concerns the fact that the resolution obtained in feedback-regulated mode looks far better than the one obtained in lift mode, at least for the cases here considered, and in contrast with the above predictions. As an example, line profiles similar to the ones of Fig. 7, but obtained in CE-FM mode, are shown in Fig. 9. The obtained resolution improvement compared to lift mode is apparent.

By the obtained results, it could be speculated that the limit resolution might be ruled by the closest approach distance (z_c in Fig. 2) rather than the average tip distance. To check this assumption, data in Fig. 8 were also plotted vs. z_c instead than vs.separation (full symbols). In this case, correspondence of experimental data with predictions (dashed and dotted lines) is improved, also for the lift mode.

It should be noticed that the value of z_c in feedback-regulated mode is negligibly small compared to oscillation amplitude, whereby z_c always reaches zero in Fig. 8 for data obtained in such mode. However, even in this case, the obtained resolution in CE-FM mode does not look consistent with the anticipations from numerical simulations of Ref. [17]. The latter discrepancy could be related to the different definitions of resolution adopted, namely, the passage through a step boundary adopted here and in Ref. [15] vs. the width of a point-like object adopted in Ref. [17]. However, different

causes for the observed resolution figures could also be possible. The roles of oscillation amplitude, closest approach distance, and feedback operation mode to determine EFM resolution on our dielectric test samples are currently under investigation.
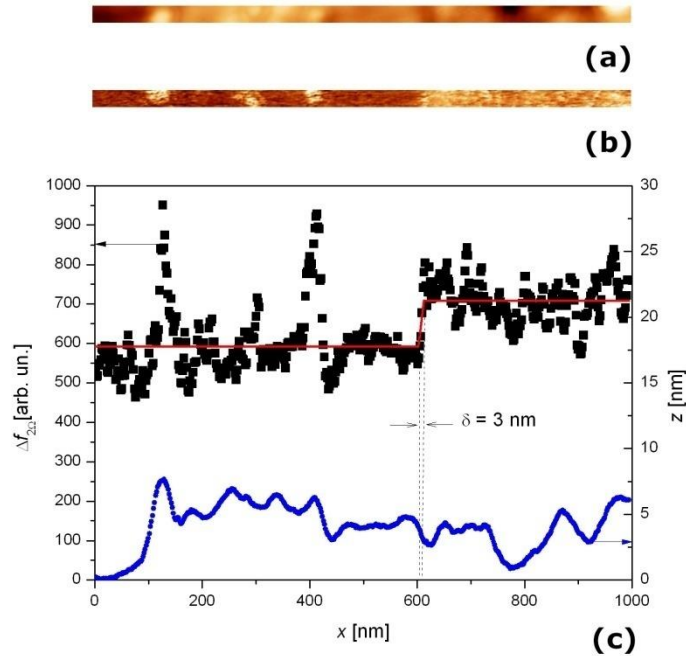
Figure 9: (a) Topography and (b) corresponding electric permittivity image of the test sample, obtained in CE-FM mode by probe "χ" (images are shown just for illustration purpose. Image width is 1000 nm, the scale bars are the same than in Fig. 6). The scanning time for these images, acquired with an oscillation amplitude $A_2 = 16.5$nm in CE-FM feedback-regulated mode, was 300s. (c) (top) Line profile taken from image (b), along with its fitting curve by the sigmoidal function of Eq. (5), showing dielectric contrast of 19.5% and lateral resolution of 3 nm. (bottom) Line profile of topography taken from image (a), showing poor correlation with the electric permittivity profile.

Conclusion. We observed a dramatic spatial resolution improvement when imaging a step-like dielectric interface by electrostatic force microscopy operated in feedback-regulated FM-AFM mode with constant oscillation amplitude, compared to the usual lift mode. This result suggests that closest approach distance z_c may rule the obtained resolution, rather than the average probe/surface distance (separation L), especially in the feedback-regulated CE-FM operation mode. Such conclusion is supported by comparison with theoretical estimations. Lateral resolutions from 3 nm

(close to the resolution limit due to sampling distance adopted in our experiment) to 10 nm, were obtained under CE-FM topography feedback, in spite of the oscillation amplitude used, of the order of 10-20 nm when operating in feedback-regulated mode. The achieved resolution range is of the order of typical correlation lengths in polymers (2-3 nm) [10,11], allowing more thorough investigations of dynamical heterogeneity effects in polymers in the real space [9].

References.

[1] Cadena MJ, Reifenberger RG, Raman A, Nanotechnology 29, 405702 (2018).

[2] Labardi M, Park JH, Nguyen HK, Prevosto D, Seong CY, Mrzel A, Scalia G, J. Non-Cryst. Solids 379, 224 (2013).

[3] Verdaguer A, Cardellach M, Segura JJ, Sacha GM, Moser J, Zdrojek M, Bachtold A, Fraxedas J, Appl. Phys. Lett. 94, 233105 (2009).

[4] Nakagiri N, Yamamoto T, Sugimura H, Suzuki Y, Miyashita M, Watanabe S, Nanotechnology 8, A32 (1997).

[5] Crider PS, Majewski MR, Zhang J, Oukris H, Israeloff NE, Appl. Phys. Lett. 91, 013102 (2007).

[6] Riedel C, Arinero R, Tordjeman P, Ramonda M, Leveque G, Schwartz GA, de Oteya DG, Alegrıa A, Colmenero J, J. Appl. Phys. 106, 024315 (2009).

[7] Labardi M, Prevosto D, Nguyen HK, Capaccioli S, Lucchesi M, Rolla PA, J. Vac. Sci. Technol. B 28, C4D11 (2010).

[8] Labardi M, Lucchesi M, Prevosto D, Capaccioli S, Appl. Phys. Lett. 108, 182906 (2016).

[9] Oukris H, Israeloff NE, Nature Physics 6, 135 (2010).

[10] Casalini R, Zhu L, Baer E, Roland CM, Polymer 88, 133 (2016).

[11] Fragiadakis D, Casalini R, Roland CM, Phys. Rev. E 84, 042501 (2011).

[12] Giessibl FJ, Rev. Mod. Phys. 75, 949 (2003).

[13] Sadewasser S, Jelinek P, Fang C-K, Custance O, Yamada Y, Sugimoto Y, Abe M, Morita S, Phys. Rev. Lett. 103, 266103 (2009).

[14] Zerweck U, Loppacher C, Otto T, Grafström S, Eng LM, Phys. Rev. B 71, 125424 (2005).

[15] Belaidi S, Lebon F, Girard P, Leveque G, Pagano S, Appl. Phys. A 66, S239 (1998).

[16] Derjaguin BV, Kolloid Zeitschrift 69, 155 (1934)

[17] Riedel C, Alegrıa A, Schwartz GA, Colmenero J, Saenz JJ, Nanotechnology 22, 285705 (2011).

[18] Maragliano C, Heskes D, Stefancich M, Chiesa M, Souier T, Nanotechnology 24, 225703 (2013).

[19] Sadeghi A, Baratoff A, Goedecker S, Phys. Rev. B 88, 035436 (2013).

[20] Zhang G, Brannum D, Dong D, Tang L, Allahyarov E, Tang S, Kodweis K, Lee J-K, Zhu L, Chem. Mater. 28, 4646 (2016).

[21] Colchero J, Gil A, Barò AM, Phys. Rev. B 64, 245403 (2001).

[22] Sacha GM, Cardellach M, Segura JJ, Moser J, Bachtold A, Fraxedas J, Verdaguer A, Nanotechnology 20, 285704 (2009).

[23] Albrecht TR, Grütter P, Horne D, Rugar D, J. Appl. Phys. 69, 668 (1991).

[24] Gil A, Colchero J, Gomez-Herrero J, Barò AM, Nanotechnology 14, 332 (2003).

[25] Hudlet S, Saint Jean M, Guthman C, Berger J, Eur. Phys. J. B 2, 5 (1998).

[26] Labardi M, Barsotti J, Prevosto D, Capaccioli S, Roland CM, Casalini R, J. Appl. Phys. 118, 224104 (2015).

[27] Bironeau A, Salez T, Miquelard-Garnier G, Sollogoub C, Macromolecules 50, 4064 (2017).

[28] Riedel C, Sweeney R, Israeloff NE, Arinero R, Schwartz GA, Alegria A, Tordjeman P, Colmenero J, Appl. Phys. Lett. 96, 213110 (2010).

[29] Ueyama H, Sugawara Y, Morita S, Appl. Phys. A 66, S295 (1998).

[30] Protasenko VV, Labardi M, Gallagher A, Phys. Rev. B 70, 245414 (2004).

[31] Takeuchi O, Ohrai Y, Yoshida S, Shigekawa H, J. J. Appl. Phys. 46, 5626 (2007).

[32] Sader JE, Jarvis SP, Appl. Phys. Lett. 84, 1801 (2004).

[33] Sacha GM, Sahagun E, Saenz JJ, J. Appl. Phys. 101, 024310 (2007).

[34] Van Der Hofstadt M, Fabregas R, Biagi MC, Fumagalli L, Gomila G, Nanotechnology 27, 405706 (2016).